


Generation of superintense isolated attosecond pulses from trapped electrons in metal surfaces

Younes Adnani

*University Ibn Tofaïl, High School of Technology, Laboratory of Electronic Systems, Information Processing, Mechanics and Energy (SETIME), Kenitra, Morocco*Abdelmalek Taoutioui *Institute for Nuclear Research, ATOMKI, 4026 Debrecen, Hungary*

Abdelkader Makhoute

Faculty of Sciences, Free University of Brussels (ULB), Campus de la Plaine, 1050 Brussels, Belgium and Dynamics of Complex Systems, Faculty of Sciences, Moulay Ismail University, B.P. 11201 Meknes, Morocco

Károly Tőkési

*Institute for Nuclear Research, ATOMKI, Debrecen, Hungary*Hicham Agueny **Department of Physics and Technology, Allegt. 55, University of Bergen, N-5007 Bergen, Norway*

(Received 19 August 2021; revised 2 March 2022; accepted 22 March 2022; published 7 April 2022)

Generation of ultrabroadband isolated attosecond pulses (IAPs) is essential for time-resolved applications in chemical and material sciences, as they have the potential to access the spectral water window region of chemical elements, which has yet to be established. Here we propose a numerical scheme for highly efficient high-order harmonic generation and hence the generation of ultrabroadband IAPs in the XUV and soft-x-ray regions. The scheme combines the use of chirped pulses with trapped electrons in copper transition-metal surfaces and takes advantage of the characteristic features of an infrared (IR) single-cycle pulse to achieve high conversion efficiencies and large spectral bandwidths. In particular, we show that ultrabroad IAPs with a duration of 370 as and with a bandwidth covering the photon energy range of 50–250 and 350–450 eV can be produced. We further show that introducing an additional IR single-cycle pulse permits us to enhance the harmonic yield in the soft-x-ray photon energy region by almost seven orders of magnitude. Our findings thus elucidate the relevance of trapped electrons in metal surfaces for developing stable and highly efficient attosecond light sources in compact solid-state devices.

DOI: [10.1103/PhysRevA.105.043104](https://doi.org/10.1103/PhysRevA.105.043104)**I. INTRODUCTION**

Recent advances of ultrafast laser technology have made it possible to produce coherent extreme-ultraviolet (XUV) radiation and attosecond pulses [1–5], which have allowed us in a pump-probe experiment to access the ultrafast microscopic processes in atoms, molecules, and solids. This fast progress has led to the emerging field of attosecond nanoscopy [6–10], which promises to open up new routes for attosecond technology, in particular, petahertz electronics [11–13] and attosecond photonics [14].

In general XUV lasers and attosecond pulses can be produced by exploiting a coherent and nonlinear optical process known as high-order harmonic generation (HHG), first reported three decades ago from the atomic gas phase [15] and now extended to solid-state systems. The HHG process from the gas phase has thus formed the basis of attosecond sci-

ence, which has now extended to the condensed-matter phase, thus offering the possibility of developing compact solid-state HHG devices. The underlying dynamics of the process in the gas phase is well established and understood on the basis of the three-step model [16–18]. The model involves tunnel ionization, free acceleration, and recombination in the presence of an oscillating electric field. These three aspects of the process are well known to be the main cause of the emission of high-frequency radiation, which manifests in the HHG spectra by odd harmonics followed by a plateau characterized by the harmonic cutoff photon energy. The latter is proportional to the driving laser intensity and inversely proportional to the square of the driving laser wavelength.

Although extensive works (e.g., [6,7,19–22]) have addressed solid-state HHG, studies of the process at the surfaces and interfaces are not well explored. Here, available studies are limited to HHG from the surface state in Cu(111) [23,24]. At the surface and interfaces, the electrons do not have enough energy to escape into the vacuum or to penetrate into the bulk as they possess energies within the band gap of a material [25].

*hicham.agueny@uib.no

Consequently, these electrons get trapped by their image potential, which is created by the polarization charge induced at the surface [25]. And because of these characteristic features, metal surfaces, unlike bulk crystals, can generate electron states classified as intrinsic surface states and image-potential states, which depend on their charge-density localization relative to the surface atomic layer [26]. As these states are localized at the outermost atomic surface layers, they are easy to manipulate, which in turn affects the physical and chemical properties of materials, thus making them of particular importance for nanotechnology and catalysis.

Despite recent achievements in solid-state HHG and in the generation of IAPs, there are still major needs in producing ultrabroad IAPs with higher flux intensities. The generated IAPs have been reported so far with limited bandwidths and mostly from bulk crystals. For instance, the predicted IAPs in recent theoretical works were found to cover the energy windows 16–20 eV in MoS₂ [27] and 20–35 and 17.5–43 eV in bulk MgO [28,29], which in general are insufficient for time-resolved measurements on unprecedented timescales.

In this paper, we demonstrate a nanoscale platform for extending the generation of IAPs to the soft-x-ray region (i.e., from 20 to 450 eV) and simultaneously increasing their flux intensities by almost seven orders of magnitude. Our scenario is based on exploiting the coherent aspect of the HHG process and makes use of a chirped pulse combined with a single-cycle pulse applied to trapped electrons in metal surfaces Cu(111) and Cu(100). In particular, we show that the predicted IAPs can be extracted with a duration of about 370 as and with a bandwidth covering the photon energy ranges 50–250 and 35–450 eV. We further show that the intensity of these pulses can be enhanced by seven orders of magnitude by introducing an IR single-cycle pulse and that the generated IAPs can be controlled by changing the surface orientations Cu(111) and Cu(100).

A key feature of our paper is exploiting the characteristics of trapped electrons in metal surfaces together with tuning the optical properties of chirped pulses combined with a single-cycle pulse. This is shown here to enhance the conversion efficiency of HHG process, unlike conventional schemes applied to periodic systems in which a fundamental multi-cycle pulse is combined with either a few-cycle pulse or a multicycle pulse. On the other hand, introducing plasmonic fields has been shown to be efficient for controlling HHG in atomic gases [30]. Our paper thus provides insights into the role of trapped electrons in metal surfaces for generating ultrabroad IAPs, which is the key for advancing attosecond science.

This paper is organized as follows. In Sec. II we present our model, which is based on solving the time-dependent Schrödinger equations (TDSEs) using a one-dimensional (1D) model, as well as its numerical implementation, which is followed by the discussion of the results of HHG and their time-frequency analysis (see Sec. III). The essence of the paper is that IAPs can be produced from image states of metal surfaces with the use of optimized chirped pulses, and their characterization can be achieved via the crystallographic orientation of the metal surface. Atomic units (a.u.), $e = m_e = 4\pi\epsilon_0 = 1$, are applied unless otherwise stated.

TABLE I. Adjustable parameters used in the analytical pseudopotential in Eq. (2) and shown in Figs. 1(a) and 1(c). The values are taken from [26]. All parameters are given in atomic units.

	a_s	A_{10}	A_1	A_2	γ
Cu(111)	3.94	−0.4371	0.1889	0.1590	2.9416
Cu(100)	3.415	−0.4218	0.2241	0.1389	2.5390

II. THEORETICAL AND COMPUTATIONAL MODELS

The coherent electron motion induced by means of light pulses in transition-metal surfaces is modeled using a 1D model with the use of an effective pseudopotential as in our previous work [24]. The 1D model has been introduced in many theoretical works (e.g., [23,31]), and it was found to provide insights into the experimental findings [31]. This minimal model is justified, as in a three-dimensional model the metal surfaces behave as a quantized 1D system in the direction perpendicular to the surface, and as a free-electron system in the direction parallel to the surface. In addition, we consider a scenario in which a linearly polarized laser pulse is directed to the [111] and [100] directions of the considered metal surface. The TDSE governing this dynamics can be written as

$$\left[-\frac{\nabla_z^2}{2} + V_{\text{ion}}(z) + H_I(t) - i\frac{\partial}{\partial t} \right] |\psi(t)\rangle = 0, \quad (1)$$

where $V_{\text{ion}}(z)$ is a one-electron pseudopotential interaction. Here, we use Chulkov potentials [26] to model the electronic structures of the metal surface's Cu:

$$V_1(z) = A_{10} + A_1 \cos\left(\frac{2\pi}{a_s}z\right), \quad z < 0, \quad (2a)$$

$$V_2(z) = -A_{20} + A_2 \cos(\gamma z), \quad 0 < z < z_1, \quad (2b)$$

$$V_3(z) = A_3 \exp[-\alpha(z - z_{\text{im}})], \quad z_1 < z < z_{\text{im}}, \quad (2c)$$

$$V_4(z) = \frac{\exp[-\lambda(z - z_{\text{im}})] - 1}{4(z - z_{\text{im}})}, \quad z_{\text{im}} < z. \quad (2d)$$

This analytical potential is characterized by the bulk inter-layer spacing a_s and the position of the image plane z_{im} . It is parametrized with A_{10} , A_1 , A_2 , and β , which are independent parameters and are given in Table I for both Cu(111) and Cu(100). These parameters are obtained by combining density-functional calculations and experiments [26]. The other parameters A_{20} , A_3 , α , z_1 , λ , and z_{im} are determined from the continuity condition of the potential and its first derivative, and are given according to [26,32]:

$$\begin{aligned} A_{20} &= A_2 - A_{10} - A_1, \quad A_3 = -A_{20} - \frac{A_2}{\sqrt{2}}, \\ z_i &= \frac{5\pi}{4\gamma}, \quad \alpha = \frac{A_2\gamma}{A_3} \sin(z_1\gamma), \\ \lambda &= 2\alpha, \quad z_{\text{im}} = z_1 - \frac{1}{\alpha} \ln\left(-\frac{\alpha}{2A_3}\right). \end{aligned} \quad (3)$$

To ensure the continuity of the pseudopotential in Eq. (2) at the boundaries, we multiply it by a damping function of the form $[1 + \tanh(z)]/2$. The time-dependent interaction $H_I(t)$

in Eq. (1) is described in the length gauge with the use of the dipole approximation

$$H_I(t) = -zS(z)[F_{\text{NIR}}(t) + F_{\text{IR}}], \quad (4)$$

where the function $S(z)$ accounts for screening of the electric field inside the Cu metal surface (see, e.g., [23,31]) and takes the form

$$S(z) = 0.5\{1 + \tanh[(6z + 3\xi)/\xi]\}. \quad (5)$$

Here ξ is the screening length. In Eq. (4), $F_{\text{NIR}}(t)$ and $F_{\text{IR}}(t)$ describe, respectively, the near-infrared (NIR) multi-cycle chirped pulses and IR single-cycle pulse. The chirped pulse has the form

$$F_{\text{NIR}}(t) = E_{\text{NIR}}f(t)\cos[\omega_{\text{NIR}}t + \phi(t)]. \quad (6)$$

The function $f(t)$ is the pulse envelope and is chosen to be of a cosine square form, ω_{NIR} is the central angular frequency, and E_{NIR} is the strength of the laser pulse. The function $\phi(t)$ in Eq. (4), which is a time-dependent carrier-envelope phase, determines the form of the chirped pulse. The latter has a hyperbolic form similar to the one used in [33],

$$\phi(t) = -\beta \tanh\left(\frac{t-t_0}{\tau}\right), \quad (7)$$

and the corresponding instantaneous frequency is obtained according to

$$\omega(t) = \omega_{\text{NIR}} - \frac{d\phi(t)}{dt} = \omega_{\text{NIR}} - \frac{\beta}{\tau} \left[\cosh^2\left(\frac{t-t_0}{\tau}\right) \right]^{-1}, \quad (8)$$

where the chirp parameters β (given in rad) and τ can be adjusted to control, respectively, the frequency sweeping range and the steepness of the chirped pulse centered at t_0 . In Eqs. (7) and (8) the optical phase $\phi(t)$ becomes zero in the case of $\beta = 0$, and thus we have $\omega(t) = \omega_{\text{NIR}}$.

The chirped pulse we use, although it can be considered idealist, is motivated by the fast progress of the use of femtosecond-laser frequency combs [34,35], which consist of a regular comb of sharp lines. This class of laser sources has the advantage of providing precise control of spectroscopy of atoms, molecules, and solid-state systems. We therefore believe that the recent achievements in optical frequency comb metrology [36] should help producing such chirped pulses in the near future.

The IR single-cycle pulse has the form as in our previous work:

$$F_{\text{IR}}(t) = E_{\text{IR}}e^{-t^2/(2\sigma_{\text{IR}}^2)}15.53\frac{t}{\tau_{\text{IR}}}, \quad (9)$$

where $\sigma_{\text{IR}} = \tau_{\text{IR}}/4\sqrt{2\ln(2)}$ is the width of the Gaussian function in Eq. (9). Here, $\tau_{\text{IR}} = 2\pi/\omega_{\text{IR}}$ and $\tau_{\text{NIR}} = 2\pi/\omega_{\text{NIR}}$ are the total duration of the IR and NIR pulses. The parameters ω_{IR} (ω_{NIR}) and E_{IR} (E_{NIR}) are, respectively, the central frequency and the strength of the IR pulse (NIR pulse). The amplitude E_i ($i = \text{NIR,IR}$) is related to the peak intensity via the relation $I_i = E_i^2$.

We calculate the HHG spectrum $H(\omega)$ by carrying out the Fourier transform of the expectation value of the dipole acceleration along the z axis:

$$H(\omega) = |D_z(\omega)|^2, \quad (10)$$

where $D_z(\omega)$ is defined by

$$D_z(\omega) = \frac{1}{\sqrt{2\pi}} \int_{t_i}^{t_f} \langle D_z(t) \rangle e^{-i\omega t} dt, \quad (11)$$

and the time-dependent expectation value of the dipole acceleration $\langle D_z(t) \rangle$ is written as

$$D_z(t) = \langle \psi(t) | \frac{\partial V(z)}{\partial z} + [F_{\text{NIR}}(t) + F_{\text{IR}}] | \psi(t) \rangle. \quad (12)$$

In Eq. (11) t_i and t_f define, respectively, the time at which the pulse is switched on and off. Note that the dipole acceleration $\langle D_z(t) \rangle$ in Eq. (12) is convoluted by a window function of a Gaussian form $\exp[-(t-t_0)^2/(2\sigma^2)]$ centered at t_0 and having the width of $\sigma=5.77/\omega_0$. The Gaussian filter has been widely used in time-frequency analysis to eliminate noises resulted from the use of the Fourier-transform algorithm. Furthermore, it allows in general a faster decaying of a desired function at the boundaries, which in our case is the dipole accelerator, thus allowing us to observe HHG plateaus with higher visibility.

In our numerical simulations the initial states are obtained by diagonalizing the matrix representation of the Hamiltonian in Eq. (1) in the absence of the laser pulse, which is constructed using a sinus-DVR basis [37]. The time evolution of the electronic wave function $\psi(t)$, which satisfies the TDSE [see Eq. (1)], is solved numerically using a split-operator method combined with a fast Fourier-transform algorithm. The calculations are carried out in a grid of size $L_z = 8190$ with the spacing grid $dz = 0.25$ a.u., i.e., $n_z=32\,768$ grid points. The time step used in the simulation is $\delta t=0.02$ a.u. The convergence is checked by performing additional calculations with twice the size of the box and a smaller time step. An absorbing boundary is employed to avoid artificial reflections, but without perturbing the inner part of the wave function. The boundary is chosen to span 10% of the grid size in the z direction.

III. RESULTS AND DISCUSSION

A. Model potential of Cu(111) and Cu(100)

We consider the metal surfaces Cu(111) and Cu(100) to be initially prepared in an image-potential state. The latter arises from the interaction of an electron in front of the surface with its positive image charge in the bulk [38,39]. The image states IS1 have the energies -0.81 and -0.57 eV, respectively, for Cu(111) and Cu(100), in accordance with the well-known formula of a hydrogenlike Rydberg series [40] $-\frac{1}{16} \frac{1}{2(n_{\text{im}}+a)^2}$, where n_{im} is the image-state index and a is a quantum defect parameter of a surface of interest. This parameter is set to be 0.02 and 0.24 for Cu(111) and Cu(100), respectively [26,39]. The energies are located above the energy Fermi level -4.62 eV and close to the top of the band gap as depicted in Figs. 1(b) and 1(d), and the corresponding electron densities are shown in Figs. 1(a) and 1(c). These electron densities exhibit a localized character of the states and are mainly confined in the metal-vacuum interface as their wave functions vanish towards the bulk as well as towards the vacuum [32]. A comparison between Cu(111) and Cu(100) shows that the maximum of the electron density of Cu(100) is shifted towards the vacuum by 2.5 a.u. compared to that

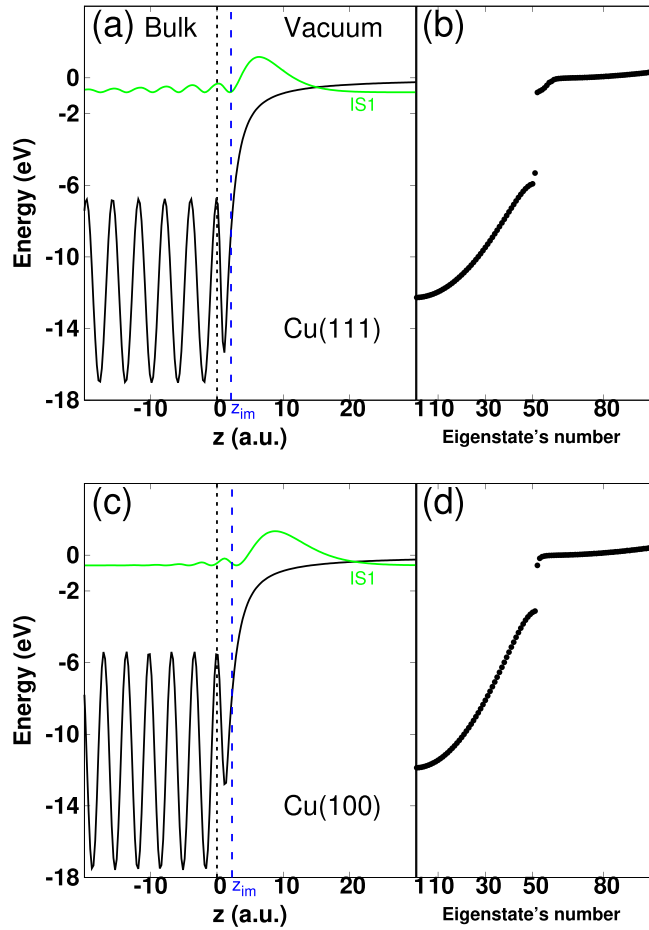


FIG. 1. Effective one-dimensional potential of Cu(111) (upper panel) and Cu(100) (lower panel) and the electron densities of the image-potential state having the energies -0.81 and -0.57 eV for Cu(111) and Cu(100), respectively. The corresponding electron densities are plotted [green (light gray) curve] with a shift from the origin to match the position of the state in the gap. (b, d) Eigenenergies at $k_{\parallel} = 0$ of the binding electronic states of the model potential in (a) and (c). Here k_{\parallel} is the crystal momentum of the electron. The pseudopotential is plotted in the limited range -20 to 30 a.u. along the z axis, and the derivative of the potential is continuous (see text).

of Cu(111). Consequently, its binding energy of the image-potential state is lowered.

B. HHG from image states in a single-color scheme

1. Effect of the chirped pulse on HHG

We first consider a scenario involving a single-color scheme in which a chirped laser pulse is linearly polarized along the [111] and [100] directions of the metal surface Cu. The pulse is characterized by a chirp parameter β and has $1.27\text{-}\mu\text{m}$ central wavelength, 43-fs pulse duration, and $2 \times 10^{13} \text{ W/cm}^2$ as the maximum of the peak intensity.

Under the use of laser pulses, most of the damages are caused by plasma effects and ablation. Based on the model proposed in [41], a value of 0.51 J/cm^2 was set as the estimated damage threshold for copper. This value was found to be close to the experimental value $0.5\text{--}0.6 \text{ J/cm}^2$ (780 nm , pulse duration of 150 fs) [42]. In our paper, the laser parameters we use correspond to a fluence of 0.32 J/cm^2 [23],

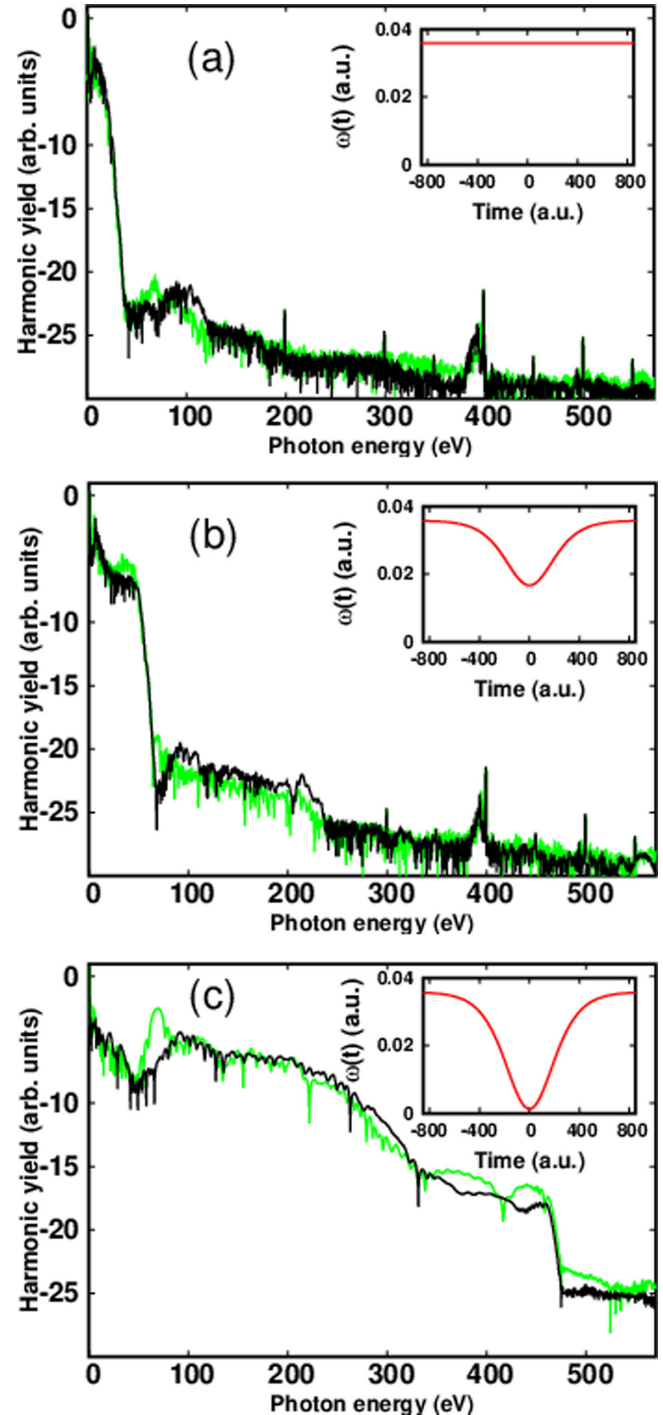


FIG. 2. HHG spectra induced by a chirped laser pulse alone calculated from the image-potential state in Cu(111) [green (light gray) curve] and Cu(100) (black curve) at different chirp parameter values: (a) $\beta = 0$, (b) $\beta = 5$, and (c) $\beta = 9$ rad. Insets show the instantaneous frequency. The spectra are plotted in logarithmic scale. The parameters of the chirped pulse are $\lambda_{\text{NIR}} = 1.27 \mu\text{m}$, $T_c = 10$ cycles, $\tau = 300$ a.u., and $I_{\text{NIR}} = 2 \times 10^{13} \text{ W/cm}^2$.

which is too low to cause any damage of the material. We therefore expect that the laser parameters we consider in this paper cannot destroy the sample.

We start our discussion by computing HHG spectra for $\beta = 0, 5$, and 9 rad for both surface orientations [111] (green

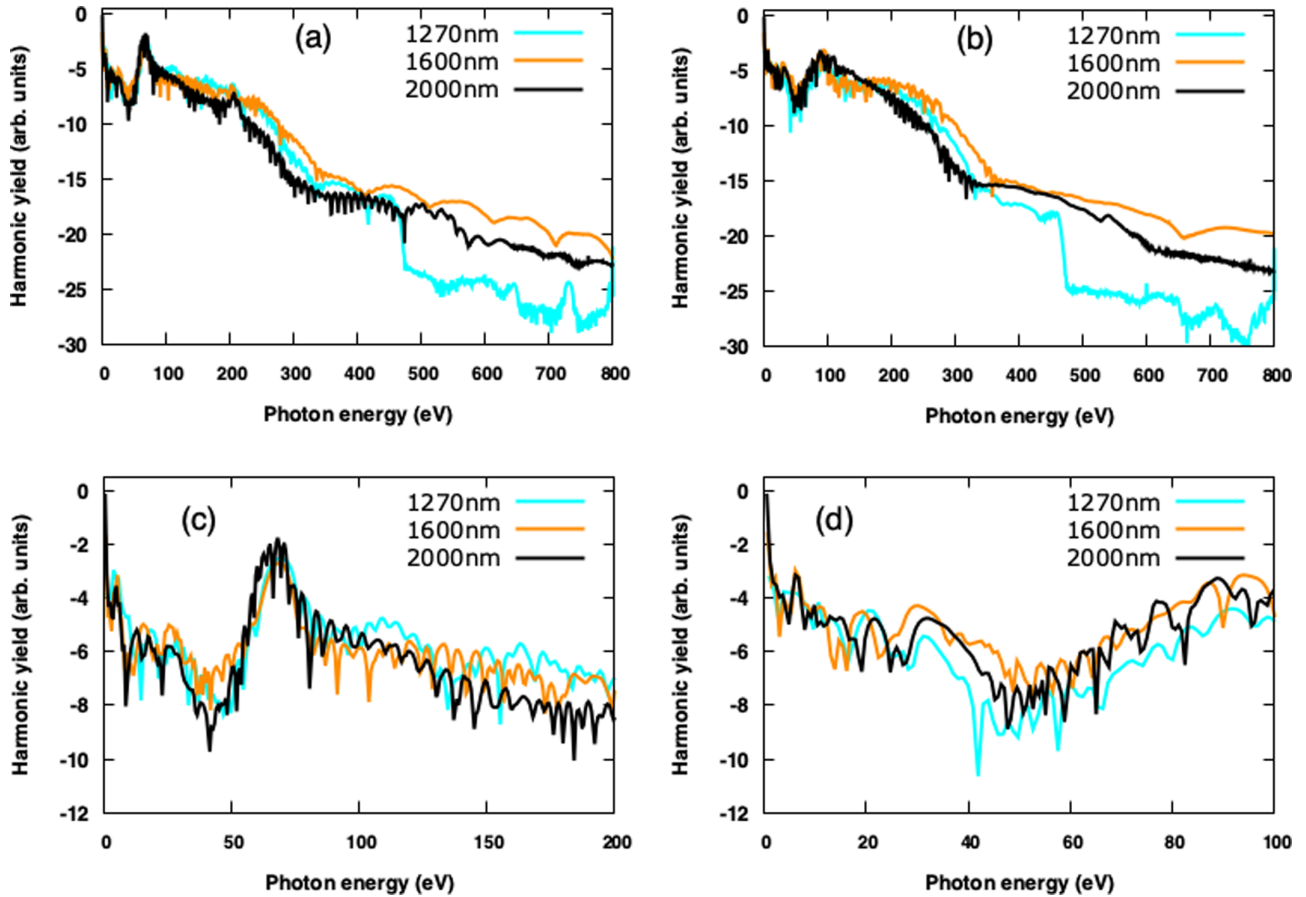


FIG. 3. HHG spectra induced by a chirped laser pulse alone calculated from the image-potential state in Cu(111) (a) and Cu(100) (b) at different wavelengths: $\lambda_{\text{NIR}} = 1.27 \mu\text{m}$ [cyan (light gray) curve], $\lambda_{\text{NIR}} = 1.6 \mu\text{m}$ (orange curve), and $\lambda_{\text{NIR}} = 2.0 \mu\text{m}$ (black curve). A zoom of the spectra in (a) and (b) is shown in (c) and (d), respectively. The spectra are plotted in logarithmic scale. The parameters of the chirped pulse are $\beta = 9 \text{ rad}$, $T_c = 10 \text{ cycles}$, $\tau = 300 \text{ a.u.}$, and $I_{\text{NIR}} = 2 \times 10^{13} \text{ W/cm}^2$.

curve) and [100] (black curve) as shown in Fig. 2. The results show a strong sensitivity of HHG spectra to the change of the chirp parameter as well as to the orientations. In particular, it is seen that the cutoff harmonic extends from $E_c = 25 \text{ eV}$ for $\beta = 0$ (free-chirp case) to $E_c = 450 \text{ eV}$ for $\beta = 9 \text{ rad}$. An extension by almost a factor of 18 is observed. This significant extension is linked to the high-kinetic energy that the free electrons acquired from the field [24]. In a classical picture, this energy is referred to as the ponderomotive energy of free electrons in an oscillating field (i.e., $U_p = I/4\omega^2$) and is inversely proportional to the instantaneous frequency characterized by the chirp parameter β . The instantaneous frequency is shown in Fig. 2 as an inset. Here one can see that increasing the parameter β results in decreasing of the frequency $\omega(t)$, and hence a vast kinetic energy U_p is transferred to free electrons, which results in an extension of the cutoff energy. A similar picture is known in HHG from atomic gases (e.g., [33]). These results, on the other hand, indicate that shaping the laser pulses by changing the chirp parameter has the advantage of amplifying the acquired energy from the laser fields.

A comparison of HHG spectra between the surface orientations [111] and [100] shows an enhancement of the harmonic yield in the case of Cu(111) by almost one order of magnitude in the photon energy range 50–100 eV. This energy range

corresponds to the XUV photon energy window, and that is an interesting finding for generating XUV IAPs with higher flux intensities in an experiment. A similar enhancement has been seen in HHG from the surface state in Cu(111) and was explained in terms of quantum-path interference. The emergence of these quantum effects in our calculations from an image-potential state and their absence in the Cu(100) case reveal the importance of trapped electrons in metal surfaces for generating and characterizing IAPs in the XUV and soft-x-ray regions. The observed enhancement is not limited to the wavelength $1.27 \mu\text{m}$, but it extends to laser wavelengths in the spectral range 1–2 μm . In this range, the above discussion remains valid. This is shown in Figs. 3(a) and 3(b), in which we present HHG spectra for 1.6 and 2.0 μm in both orientations Cu(111) and Cu(100).

A closer inspection of the spectra at low photon energy [see Figs. 3(c) and 3(d)] reveals some similarities in the behavior of HHG for the wavelengths considered here. This behavior is found to be sensitive to the surface orientation of the metal. The investigation of its origin is however beyond the scope of the present paper, which calls for additional works to shed light on this observed behavior. On the other hand, one can see that beyond the photon energy 400 eV the spectra exhibit a fast oscillatory structure. In order to rule out that their origin is caused by numerical noise, we have performed calculations

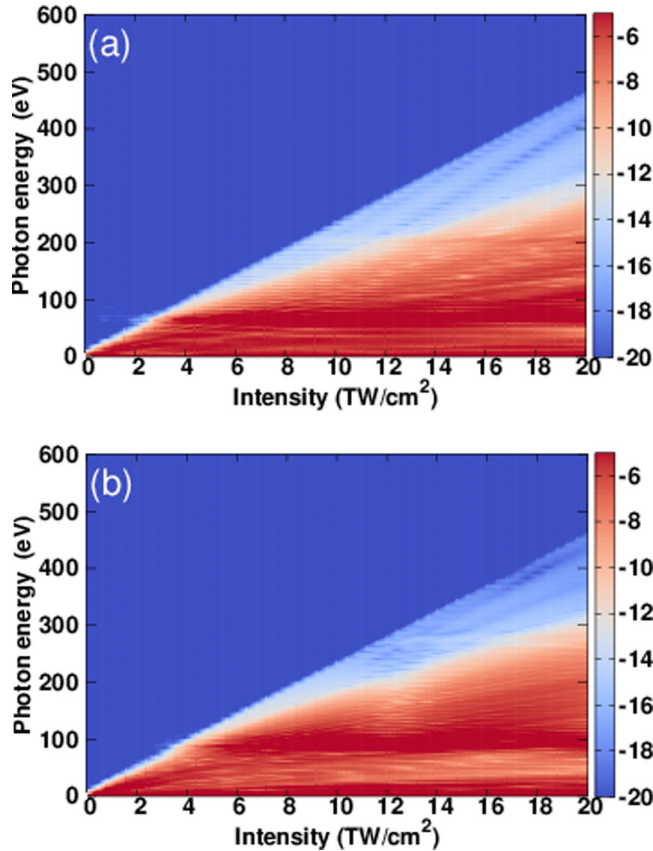


FIG. 4. Two-dimensional HHG spectra induced by a chirped laser pulse at different peak intensities in the range 0.5–20 TW/cm^2 . The spectra are calculated from the image-potential state in Cu(111) (a) and Cu(100) (b). The spectra are plotted in logarithmic scale and are given in arb. units. The parameters of the chirped pulse are $\beta = 9$ rad, $\lambda_{\text{NIR}} = 1.27 \mu\text{m}$, $T_c = 10$ cycles, and $\tau = 300$ a.u..

with a larger spatial grid of $L_z = 16380$ a.u. ($n_z = 65536$ points) and a smaller time step (i.e., $\Delta = 0.02$ a.u.); the results are found to be indistinguishable as shown in Supplemental Material [43], thus ensuring their convergence. Furthermore, we have observed that beyond the laser wavelength $2 \mu\text{m}$, the HHG efficiency decreases similarly to the case of gases (see Supplemental Material [43]).

2. Effect of the peak intensity on HHG

Additional calculations illustrating the effect of varying the peak intensity of the chirped pulse on the HHG spectra are displayed in Fig. 4. We use the same parameters as in Fig. 2(c). The results are shown for both surface orientations [111] and [100], respectively, in Figs. 4(a) and 4(b). As expected, the photon energy cutoff increases linearly as a function of the peak intensity and follows the approximative formula

$$E_{\text{max}}(\beta) = I_p + 3.17U_p(\beta), \quad (13)$$

where I_p is the ionization potential. The formula (13) deviates from the well-known one due to its dependence on the chirp parameter β via the instantaneous frequency $\omega(t)$. It was found however that this formula reproduces very well the en-

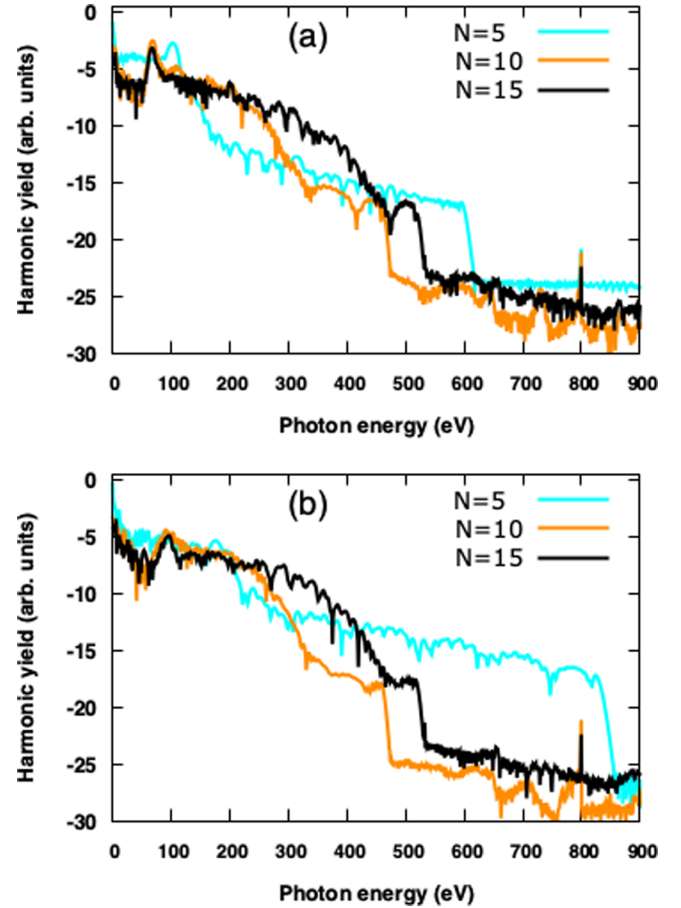


FIG. 5. HHG spectra induced by a chirped laser pulse alone calculated from the image-potential state in Cu(111) (a) and Cu(100) (b) at different number of cycles: $N = 5$ cycles [cyan (light gray) curve], $N = 10$ cycles (orange curve), and $N = 15$ cycles (black curve). The spectra are plotted in logarithmic scale. The parameters of the chirped pulse are $\beta = 9$ rad, $\lambda_{\text{NIR}} = 1.27 \mu\text{m}$, $T_c = 10$ cycles, $\tau = 300$ a.u., and $I_{\text{NIR}} = 2 \times 10^{13} \text{ W}/\text{cm}^2$.

ergy cutoff by including some adjustments to take into account the instantaneous variation of the kinetic energy U_p [24].

In Fig. 4, it is seen that the linear behavior of the energy cutoff is found to be sensitive to the surface orientations Cu(111) and Cu(100). This is expected as the initial state exhibits some differences in both the bulk and vacuum regions as described above [see Figs. 1(a) and 1(c)], which in turn modify the HHG spectra. We stress here that the observed linear scaling has been already observed in the chirp-free case [23] and found to be caused by the electron traveling through energy dispersion bands [44].

3. Effect of the pulse duration on HHG

In order to investigate how the pulse duration modifies the HHG spectra, we perform calculations at two different durations of the chirped pulse for both Cu(111) [see Fig. 5(a)] and Cu(100) [see Fig. 5(b)]: five cycles [cyan (light gray) curve] and 15 cycles (black curve). For reference, the spectra obtained with ten-cycle pulses are also shown in the same figure with orange color. These pulses correspond to a duration

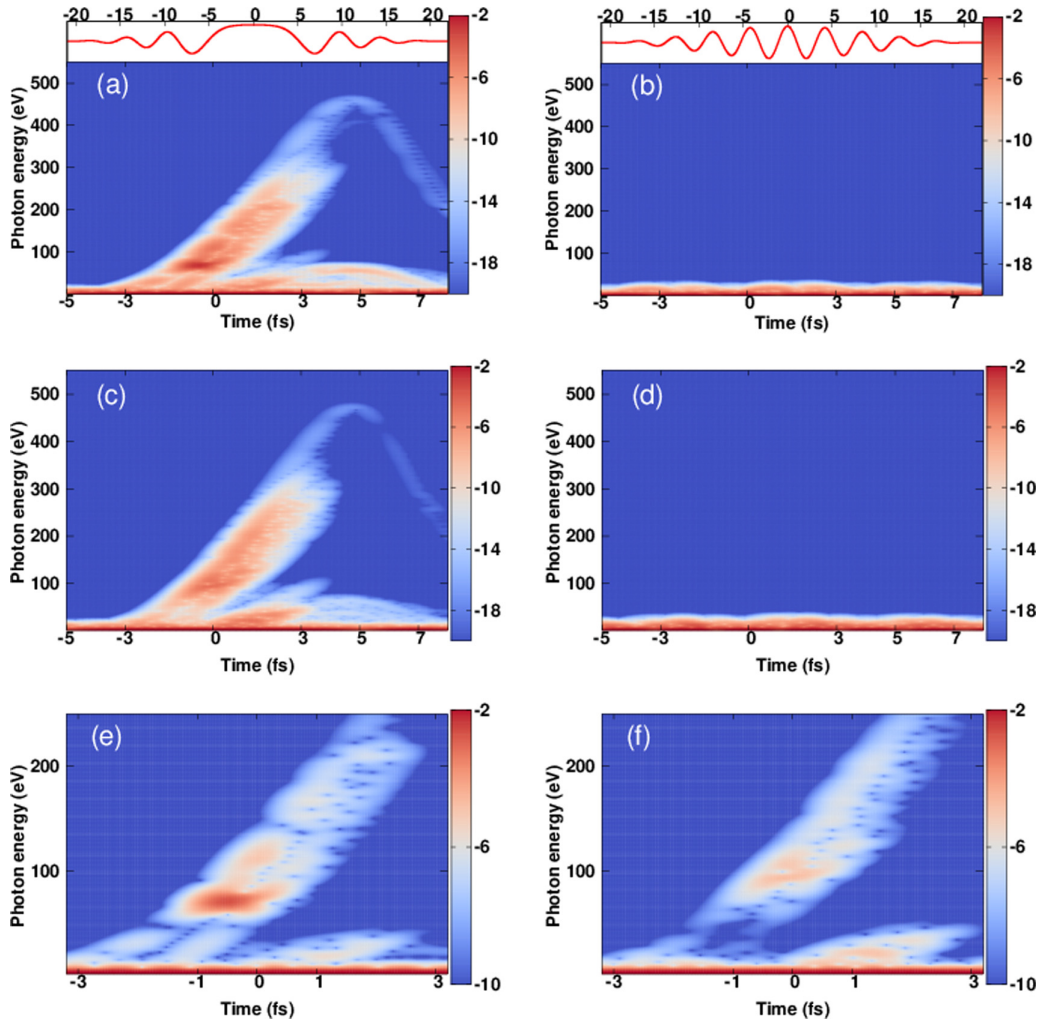


FIG. 6. Time-frequency analysis of the harmonic spectra for Cu(111) (upper panel) and Cu(100) (middle panel). A zoom of the spectra in (a) and (b) in the photon energy 1–250 eV and time interval -3 to 3 fs is shown in the lower panel for Cu(111) (e) and Cu(100) (f). For reference, the spectra for $\beta = 0$ for Cu(111) (b) and Cu(100) (d) are also shown. Insets: The form of the chirped pulse (a) and free-chirped pulse (b). The spectra are plotted in logarithmic scale and are given in arb. units. The parameters of the chirped pulse are $\lambda_{\text{NIR}} = 1.27 \mu\text{m}$, $T_c = 10$ cycles, $\tau = 300$ a.u., and $I_{\text{NIR}} = 2 \times 10^{13} \text{ W/cm}^2$.

of 21.18, 42.36, and 63.54 fs, respectively, for 5-, 10-, and 15-cycle pulses. The results are shown for the laser wavelength $1.27 \mu\text{m}$ and at the peak intensity of 2 TW/cm^2 . The chirp parameter is fixed at $\beta = 9$. It is seen that changing the pulse duration modifies dramatically the harmonic yield as well as the photon energy cutoff. All the spectra exhibit an interesting signature that reflects the dynamics behind the change of the pulse duration. It is found that the shorter pulse with five cycles induces a substantial extension of the photon energy cutoff, in particular for the surface orientation [100], in which higher photon energies up to 850 eV are generated. A similar behavior has been observed for the Cu(111)-NaCl system using a chirp-free pulse [23]. On the other hand, an enhancement of the harmonic yield by two orders of magnitude is observed at the photon energy 100 eV for the geometry [111], whereas the use of a longer pulse with 15 cycles is not optimal for producing interesting results when compared with the spectra for five- and ten-cycle pulses.

4. Time-frequency analysis of HHG

In the following our results will be presented for the laser wavelength $1.27 \mu\text{m}$ and at the peak intensity of 2 TW/cm^2 . Here, we adopt a Gabor time-frequency profile of HHG and extract amplitudes of harmonics in the XUV and soft-x-ray regions. This Gabor-based analysis is widely performed in connection with the HHG process in atomic and molecular gases as well as solids. It has the advantage of providing detailed information about the time emission of the bursts and thus allowing us to access the width of the generated attosecond pulses. We thus perform this analysis for both orientations Cu(111) and Cu(100) in the case of a chirped [see Figs. 6(a) and 6(c)] and unchirped pulses [see Figs. 6(b) and 6(d)]. The obtained results are displayed for a peak intensity of $2 \times 10^{13} \text{ W/cm}^2$ and for a fixed chirp parameter of $\beta = 9$ rad. The figure provides a comparative overview of the role of chirped pulses as well as the surface orientation for spectral characterizations of emission bursts.

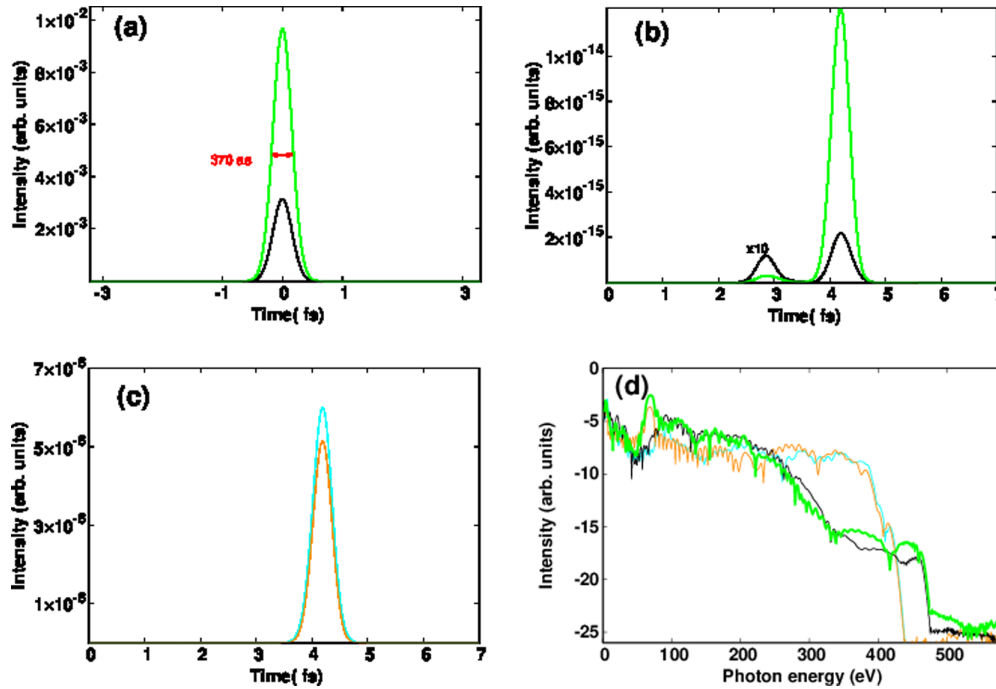


FIG. 7. Upper panel: Intensity of the extracted IAPs with the chirped pulse alone for Cu(111) [green (light gray) curve] and Cu(100) (black curve) at two different window energies: (a) 50–250 eV and (b) 350–450 eV. The amplitude of IAPs for Cu(100) in (b) is multiplied by 10 to make it visible. The width of the IAPs is indicated in (a). (c) Intensity of IAPs in the presence of a single cycle for Cu(111) (orange curve) and Cu(100) [cyan (light gray) curve]. (d) The corresponding HHG spectra displayed with the same colors as in (a) and (c). The green curve in (d) is displayed with a thick line. The parameters of the chirped pulse are $\lambda_{\text{NIR}} = 1.27 \mu\text{m}$, $T_c = 10$ cycles, $\beta = 9$ rad, and $I_{\text{NIR}} = 2 \times 10^{13} \text{ W/cm}^2$. The parameters of the IR single-cycle pulse are $\lambda_{\text{IR}} = 12.7 \mu\text{m}$ and $I_{\text{IR}} = 1 \times 10^{12} \text{ W/cm}^2$.

In particular, one can see the emission of a pronounced burst in both orientations of Cu, while it is absent in the free-chirped case. The emission bursts extend to higher energies and up to 450 eV when shaping the laser pulses and are mostly generated in the time interval -3 to 3 fs. The emitted bursts look similar for both surface orientations. A closer inspection of the spectra however reveals some distinct features that emerge with higher visibility in the time interval -1.5 to 0.5 fs as shown in Figs. 6(e) and 6(f) for Cu(111) and Cu(100), respectively. These features encode information about the electronic band structure of the metal surface having a specific orientation, which in turn can be mapped out in the generated IAPs.

C. Isolated attosecond pulses in a two-color scheme

Based on the Gabor analysis displayed in Fig. 6, we extract the intensities of the harmonics covering a broad window energy as defined below. Specifically, we compute a coherent sum of the consecutive harmonics in a well-defined energy region according to [45,46]

$$I_z(\tau) = \left| \frac{1}{\sqrt{2\pi}} \sum_{\omega_i}^{\omega_f} \int_{t_i}^{t_f} \exp\left[-\frac{(t-\tau)^2}{2\sigma^2}\right] \langle D_z(t) \rangle e^{-i\omega t} dt \right|^2, \quad (14)$$

where ω_i and ω_f represent the energy window used for extracting the intensity of IAPs. The results are presented in Fig. 7 and display the extracted IAPs having a broad bandwidth covering the energy window 50–250 eV [see Fig. 7(a)] and 350–450 eV [see Fig. 7(b)]. These regions are chosen to

cover regular high-energy plateaus emerging in HHG spectra as shown in Fig. 2(c). Here, the duration of the extracted IAPs is found to be about 370 as for both surface orientations [111] and [100]. However, the intensity of IAPs is one order of magnitude higher in the [111] orientation case. An extension of the extraction procedure to a broader energy window (i.e., 350–450 eV) shows the appearance of a burst with a weak intensity [see Fig. 7(b)].

In order to enhance its intensity we introduce an additional IR single-cycle pulse with a peak intensity of $1 \times 10^{12} \text{ W/cm}^2$ and central wavelength of $\lambda_{\text{IR}} = 10\lambda_{\text{NIR}}$. The use of such pulses is motivated by the recent work [47] in which the authors demonstrate the possibility of producing IR single-cycle pulses covering the spectral range 5–14 μm and with the intensity of the order of TW/cm^2 .

The basic physics behind these single-cycle pulses is related to a high-momentum transfer to electrons [48–50], which results in a high-energy recollision, and hence extension of the harmonic cutoff and enhancement of the harmonic yields as it has been discussed recently in the context of an atomic system [51]. The effect of introducing an IR single-cycle pulse on HHG can be seen in Fig. 7(d). Interestingly enough, an enhancement of the harmonic yield by almost seven orders of magnitude is seen in both surface orientations Cu(111) (orange curve) and Cu(100) [cyan (light gray) curve]. For reference, the HHG spectra obtained with the chirped pulse alone are also shown in the same figure. This enhancement is reflected in the extracted IAPs as one can see in Fig. 7(c). These IAPs are generated with roughly the same intensity, unlike in the case with only the chirped pulses. This

result elucidates the effect of introducing an IR single-cycle pulse to enhance the intensity of the IAPs in the soft-x-ray photon energy region. Generating IAPs in this region is highly desirable for time-resolved measurements with attosecond precision.

At this point we conclude that the localized aspect of image-potential states combined with tuning the optical properties of chirped pulses and the use of a single-cycle pulse are found to be relevant for generating ultrabroad IAPs with larger bandwidths. Although the role of localized states has been addressed previously, it has been done by creating a vacancy in a periodic system that is initially prepared in bulk states (delocalized states) [52]. Our paper, however, addresses this role from a different perspective: the dynamics is initiated from a localized state (image-potential state) in a scenario involving two different geometries [Cu(111) and Cu(100)], which leave their imprint in the HHG spectra. We note that such geometrical dependence in HHG has been reported previously in ferromagnetic monolayers [53]. Our paper thus complements the existing studies and adds insights on the role of localized states in solid-state HHG.

With state-of-the-art laser technology, it should be possible to generate IR single-cycle pulses with petawatt peak intensities and in the spectral range considered in our present paper. For instance, a new scheme capable of producing relativistic wavelength-tunable single-cycle pulses (514 μm) has been proposed [47,54,55]. On the other hand, producing chirped femtosecond pulses should be possible using current state-of-the-art techniques, which benefit from modern-day ultrafast laser technologies (e.g., [56]). A widely used technique that is considered as a standard laser configuration is chirped pulse amplification [57], which is based on the stretching and compression of the laser pulse. In this technique, the control of the chirped pulse can be achieved using for instance active devices such as deformable mirrors or liquid crystal arrays [58,59]. On the other hand, generating positive chirp, as in our paper, can be done in an experiment using an imperfect dispersion compensation [59], which can be achieved by tuning either a pulse stretcher or a pulse compressor. Furthermore, the

characterization of the chirped pulse can be realized using frequency-resolved optical gating technique [60]. We thus believe that the two-color scheme proposed in our paper to generate XUV and soft-x-ray IAPs should be experimentally feasible in the near future. On the other hand, despite the difficulties in realizing an experiment of the HHG process from metal surfaces [61,62], our paper provides insights into their role for coherent control of the process. It thus functions as a benchmark for future studies of solid-state HHG and in general of strong-field light-matter interaction.

IV. CONCLUSIONS

In conclusion, we have demonstrated the relevance of trapped electrons in metal surfaces for generating ultrabroad IAPs when they are excited by means of optimized chirped pulses combined with an IR single-cycle pulse. In particular, we have predicted the generation of IAPs with a duration of about 370 as and with a bandwidth covering the photon energy of 50–250 and 350–450 eV. The generated IAPs were found to be sensitive to the surface orientations Cu(111) and Cu(100), which suggest their use for characterizing the IAPs. Moreover, we have shown the effect of introducing an IR single-cycle pulse for enhancing the intensity of the extracted soft-x-ray IAPs. We have found an enhancement by a factor of seven orders of magnitude compared to the case with the chirped pulse alone. Our findings thus indicate the relevance of trapped electrons excited by a two-color scheme for extending attosecond metrology to the XUV and soft-x-ray regions. This extension is critical towards harnessing attosecond quantum technologies from solid-state systems.

ACKNOWLEDGMENTS

A.Y. acknowledges support from SPIRE during his stay at the University of Bergen. A.T. acknowledges support from the bilateral relationships between Morocco and Hungary in Science and Technology under Project No. 2018-2.1.10-TÉT-MC-2018-00008.

-
- [1] M. Hentschel, R. Kienberger, C. Spielmann, G. A. Reider, N. Milosevic, T. Brabec, P. Corkum, U. Heinzmann, M. Drescher, and F. Krausz, Attosecond metrology, *Nature (London)* **414**, 509 (2001).
 - [2] P. Corkum and F. Krausz, Attosecond science, *Nat. Phys.* **3**, 381 (2007).
 - [3] F. Krausz and M. Ivanov, Attosecond physics, *Rev. Mod. Phys.* **81**, 163 (2009).
 - [4] F. Krausz and M. I. Stockman, Attosecond metrology: From electron capture to future signal processing, *Nat. Photonics* **8**, 205 (2014).
 - [5] J. Li, J. Lu, A. Chew, S. Han, J. Li, Y. Wu, H. Wang, S. Ghimire, and Z. Chang, Attosecond science based on high harmonic generation from gases and solids, *Nat. Commun.* **11**, 2748 (2020).
 - [6] S. Ghimire, A. D. DiChiara, E. Sistrunk, P. Agostini, L. F. DiMauro, and D. A. Reis, Observation of high-order harmonic generation in a bulk crystal, *Nat. Phys.* **7**, 138 (2011).
 - [7] G. Vampa, T. J. Hammond, N. Thiré, B. E. Schmidt, F. Légaré, C. R. McDonald, T. Brabec, and P. B. Corkum, Linking high harmonics from gases and solids, *Nature (London)* **522**, 462 (2015).
 - [8] M. F. Ciappina, J. A. Pérez-Hernández, A. S. Landsman, W. A. Okell, S. Zherebtsov, B. Förg, J. Schötz, L. Seiffert, T. Fennel, T. Shaaran, T. Zimmermann, A. Chacón, R. Guichard, A. Zair, J. W. G. Tisch, J. P. Marangos, T. Witting, A. Braun, S. A. Maier, L. Roso *et al.*, Attosecond physics at the nanoscale, *Rep. Prog. Phys.* **80**, 054401 (2017).
 - [9] G. Vampa and T. Brabec, Merge of high harmonic generation from gases and solids and its implications for attosecond science, *J. Phys. B* **50**, 083001 (2017).
 - [10] H. Lakhota, H. Y. Kim, M. Zhan, S. Hu, S. Meng, and E. Goulielmakis, Laser picoscopy of valence electrons in solids, *Nature (London)* **583**, 55 (2020).
 - [11] M. Garg, M. Zhan, T. T. Luu, H. Lakhota, T. Klostermann, A. Guggenmos, and E. Goulielmakis, Multi-petahertz

- electronic metrology, *Nature (London)* **538**, 359 (2016).
- [12] J. Schoetz, Z. Wang, M. Pisanty, E. Lewenstein, M. F. Kling, and M. F. Ciappina, Perspective on petahertz electronics and attosecond nanoscopy, *ACS Photonics* **6**, 3057 (2019).
- [13] Y. Yang, M. Turchetti, P. Vasireddy, W. P. Putnam, O. Karnbach, A. Nardi, K. X. Krtner, K. K. Berggren, and P. D. Keathley, Light phase detection with on-chip petahertz electronic networks, *Nat. Commun.* **11**, 3407 (2020).
- [14] D. Ghimire and S. Reis, High-harmonic generation from solids, *Nat. Phys.* **15**, 10 (2019).
- [15] M. Ferray, A. L'Huillier, X. Li, L. Lompre, G. Mainfray, and C. Manus, Multiple-harmonic conversion of 1064 nm radiation in rare gases, *J. Phys. B* **21**, L31 (1988).
- [16] P. B. Corkum, Plasma Perspective on Strong Field Multiphoton Ionization, *Phys. Rev. Lett.* **71**, 1994 (1993).
- [17] K. J. Schafer, B. Yang, L. F. DiMauro, and K. C. Kulander, Above Threshold Ionization Beyond the High Harmonic Cutoff, *Phys. Rev. Lett.* **70**, 1599 (1993).
- [18] M. Lewenstein, P. Balcou, M. Y. Ivanov, A. L'Huillier, and P. B. Corkum, Theory of high-harmonic generation by low-frequency laser fields, *Phys. Rev. A* **49**, 2117 (1994).
- [19] B. Zaks, R. B. Liu, and M. S. Sherwin, Experimental observation of electron-hole recollisions, *Nature (London)* **483**, 580 (2012).
- [20] G. Vampa, T. J. Hammond, N. Thiré, B. E. Schmidt, F. Légaré, C. R. McDonald, T. Brabec, D. D. Klug, and P. B. Corkum, All-Optical Reconstruction of Crystal Band Structure, *Phys. Rev. Lett.* **115**, 193603 (2015).
- [21] M. Hohenleutner, F. Langer, O. Schubert, M. Knorr, U. Huttner, S. W. Koch, M. Kira, and R. Huber, Real-time observation of interfering crystal electrons in high-harmonic generation, *Nature (London)* **523**, 572 (2015).
- [22] Y. S. You, D. A. Reis, and S. Ghimire, Anisotropic high-harmonic generation in bulk crystals, *Nat. Phys.* **13**, 345 (2017).
- [23] N. F. Aguirre and F. Martín, Tuning high-harmonic generation by controlled deposition of ultrathin ionic layers on metal surfaces, *Phys. Rev. B* **94**, 245423 (2016).
- [24] H. Agueny, Tuning the electronic band structure of metal surfaces for enhancing high-order harmonic generation, *J. Chem. Phys.* **154**, 244702 (2021).
- [25] P. M. Echenique and J. B. Pendry, Plasmon effects on image states at metal surfaces, *J. Phys. C* **19**, 5437 (1986).
- [26] E. Chulkov, V. Silkin, and P. Echenique, Image potential states on metal surfaces: Binding energies and wave functions, *Surf. Sci.* **437**, 330 (1999).
- [27] M. Guan, S. Hu, H. Zhao, C. Lian, and S. Meng, Toward attosecond control of electron dynamics in two-dimensional materials, *Appl. Phys. Lett.* **116**, 043101 (2020).
- [28] T.-J. Shao, L.-J. Lü, J.-Q. Liu, and X.-B. Bian, Quantum path interferences and selection in interband solid high-order harmonic generation in mgo crystals, *Phys. Rev. A* **101**, 053421 (2020).
- [29] Z. Nourbakhsh, N. Tancogne-Dejean, H. Merdji, and A. Rubio, High harmonics and isolated attosecond pulses from MgO, *Phys. Rev. Appl.* **15**, 014013 (2021).
- [30] I. N. Ansari, M. S. Mrudul, M. F. Ciappina, M. Lewenstein, and G. Dixit, Simultaneous control of harmonic yield and energy cutoff of high-order harmonic generation using seeded plasmonically enhanced fields, *Phys. Rev. A* **98**, 063406 (2018).
- [31] A. K. Kazansky and P. M. Echenique, One-Electron Model for the Electronic Response of Metal Surfaces to Subfemtosecond Photoexcitation, *Phys. Rev. Lett.* **102**, 177401 (2009).
- [32] E. So, J. A. Gibbard, and T. P. Softley, Ionization of Rydberg h atoms at band-gap metal surfaces via surface and image states, *J. Phys. B* **48**, 175205 (2015).
- [33] J. J. Carrera and Shih-I Chu, Extension of high-order harmonic generation cutoff via coherent control of intense few-cycle chirped laser pulses, *Phys. Rev. A* **75**, 033807 (2007).
- [34] L. Chang, S. Liu, and J. E. Bowers, Integrated optical frequency comb technologies, *Nat. Photonics* **16**, 95 (2022).
- [35] S. T. Cundiff and J. Ye, Colloquium: Femtosecond optical frequency combs, *Rev. Mod. Phys.* **75**, 325 (2003).
- [36] T. Udem, R. Holzwarth, and T. W. Hänsch, Optical frequency metrology, *Nature (London)* **416**, 233 (2002).
- [37] J. Lill, G. Parker, and J. Light, Discrete variable representations and sudden models in quantum scattering theory, *Chem. Phys. Lett.* **89**, 483 (1982).
- [38] P. M. Echenique and J. B. Pendry, The existence and detection of Rydberg states at surfaces, *J. Phys. C* **11**, 2065 (1978).
- [39] T. Klamroth, P. Saalfrank, and U. Höfer, Open-system density-matrix approach to image-potential dynamics of electrons at cu(100): Energy- and time-resolved two-photon photoemission spectra, *Phys. Rev. B* **64**, 035420 (2001).
- [40] P. Echenique and J. Pendry, Theory of image states at metal surfaces, *Prog. Surf. Sci.* **32**, 111 (1989).
- [41] E. G. Gamaly, A. V. Rode, B. Luther-Davies, and V. T. Tikhonchuk, Ablation of solids by femtosecond lasers: Ablation mechanism and ablation thresholds for metals and dielectrics, *Phys. Plasmas* **9**, 949 (2002).
- [42] C. Momma, S. Nolte, B. N. Chichkov, F. v. Alvensleben, and A. Tnnermann, Precise laser ablation with ultrashort pulses, *Appl. Surf. Sci.* **109–110**, 15 (1997).
- [43] See Supplemental Material at <http://link.aps.org/supplemental/10.1103/PhysRevA.105.043104> for further discussion on the behavior of HHG spectra at high photon energies,
- [44] G. Vampa, C. R. McDonald, G. Orlando, P. B. Corkum, and T. Brabec, Semiclassical analysis of high harmonic generation in bulk crystals, *Phys. Rev. B* **91**, 064302 (2015).
- [45] Y. Mairesse, A. de Bohan, L. J. Frasinski, H. Merdji, L. C. Dinu, P. Monchicourt, P. Breger, M. Kovačev, R. Taïeb, B. Carré, H. G. Muller, P. Agostini, and P. Salières, Attosecond synchronization of high-harmonic soft x-rays, *Science* **302**, 1540 (2003).
- [46] P. Lan, P. Lu, W. Cao, X. Wang, and G. Yang, Phase-locked high-order-harmonic and sub-100-as pulse generation from stretched molecules, *Phys. Rev. A* **74**, 063411 (2006).
- [47] Z. Nie, C.-H. Pai, J. Hua, C. Zhang, Y. Wu, Y. Wan, F. Li, J. Zhang, Z. Cheng, Q. Su, S. Liu, Y. M. Xiaonan Ning, Y. He, W. Lu, H.-H. Chu, J. Wang, W. B. Mori, and C. Joshi, Relativistic single-cycle tunable infrared pulses generated from a tailored plasma density structure, *Nat. Photonics* **12**, 489 (2018).
- [48] S. Li and R. R. Jones, Ionization of Excited Atoms by Intense Single-Cycle THz Pulses, *Phys. Rev. Lett.* **112**, 143006 (2014).
- [49] B. C. Yang and F. Robicheaux, Field-ionization threshold and its induced ionization-window phenomenon for rydberg atoms in a short single-cycle pulse, *Phys. Rev. A* **90**, 063413 (2014).

- [50] M. Chovancova, H. Agueny, J. J. Rørstad, and J. P. Hansen, Classical and quantum-mechanical scaling of ionization from excited hydrogen atoms in single-cycle thz pulses, *Phys. Rev. A* **96**, 023423 (2017).
- [51] A. Taoutioui and H. Agueny, Femtosecond single cycle pulses enhanced the efficiency of high order harmonic generation, *Micromachines* **12**, 610 (2021).
- [52] M. Mrudul, N. Tancogne-Dejean, A. Rubio, and G. Dixit, High-harmonic generation from spin-polarised defects in solids, *npj Comput. Mater.* **6**, 10 (2020).
- [53] G. Zhang, M. Si, M. Murakami, Y. Bai, and T. F. George, Generating high-order optical and spin harmonics from ferromagnetic monolayers, *Nat. Commun.* **9**, 1 (2018).
- [54] X.-L. Zhu, S.-M. Weng, M. Chen, Z.-M. Sheng, and J. Zhang, Efficient generation of relativistic near-single-cycle mid-infrared pulses in plasmas, *Light: Sci. Appl.* **9**, 46 (2020).
- [55] F. Ma, H. Liu, N. Huang, and Q. Sun, Generation of single-cycle mid-infrared pulses via coherent synthesis, *Opt. Express* **20**, 28455 (2012).
- [56] D. Gauthier, E. Allaria, M. Coreno, I. Cudin, H. Dacasa, M. B. Danailov, A. Demidovich, S. Di Mitri, B. Diviacco, E. Ferrari *et al.*, Chirped pulse amplification in an extreme-ultraviolet free-electron laser, *Nat. Commun.* **7**, 13688 (2016).
- [57] D. Strickland and G. Mourou, Compression of amplified chirped optical pulses, *Opt. Commun.* **56**, 219 (1985).
- [58] F. X. Kärtner, U. Morgner, R. Ell, T. Schibli, J. G. Fujimoto, E. P. Ippen, V. Scheuer, G. Angelow, and T. Tschudi, Ultra-broadband double-chirped mirror pairs for generation of octave spectra, *J. Opt. Soc. Am. B* **18**, 882 (2001).
- [59] K.-H. Hong, J. H. Sung, Y. S. Lee, and C. H. Nam, Temporal characterization of chirped femtosecond laser pulses, *Opt. Commun.* **213**, 193 (2002).
- [60] T. S. Clement, A. J. Taylor, and D. J. Kane, Single-shot measurement of the amplitude and phase of ultrashort laser pulses in the violet, *Opt. Lett.* **20**, 70 (1995).
- [61] S. Ghimire, G. Ndabashimiye, A. D. DiChiara, E. Sistrunk, M. I. Stockman, P. Agostini, L. F. DiMauro, and D. A. Reis, Strong-field and attosecond physics in solids, *J. Phys. B* **47**, 204030 (2014).
- [62] A. Korobenko, S. Saha, A. T. Godfrey, M. Gertsvolf, A. Y. Naumov, D. M. Villeneuve, A. Boltasseva, V. M. Shalaev, and P. B. Corkum, High-harmonic generation in metallic titanium nitride, *Nat. Commun.* **12**, 4981 (2021).